Dalton Transactions

ROYAL SOCIETY OF CHEMISTRY

PAPER

View Article Online
View Journal | View Issue

Cite this: *Dalton Trans.*, 2021, **50**, 10737

A systematic study of the influence of ligand field on the slow magnetic dynamics of Co(II)-diimine compounds†

Indrani Bhowmick, [a] Brian S. Newell [a,b] and Matthew P. Shores *[a]

Herein we report heteroleptic Co(II) diimine complexes $[Co(H_2bip)_2Cl_2]$ (**1**), $[Co(H_2bip)_2Br_2]$ (**2**), $[Co(H_2bip)_3]Br_2{\cdot}1MeOH$ (**3**) and $[Co(H_2bip)_2(Me_2bpy)]Br_2{\cdot}(MeCN)_{0.5}{\cdot}(H_2O)_{0.25}$ (**4**) (H_2bip = 2,2′-bi-1,4,5,6-tetrahydropyrimidine, bpy = 2,2′-dipyridyl, Me_2bpy = 4,4′-Me-2,2′-dipyridyl), purposefully prepared to enable a systematic study of magnetic property changes arising from the increase of overall ligand field from σ/π-donor chlorido (**1**) to π-acceptor 4,4′Me-2,2′bpy (**4**). The presence of axial and rhombic anisotropy (*D* and *E*) of these compounds is sufficient to allow **1–4** to show field-induced slow relaxation of magnetization. Interestingly, we found as the effective ligand field is increased in the series, rhombicity (*E*/*D*) decreases, and the magnetic relaxation profile changes significantly, where relaxation of magnetization at a specific temperature becomes gradually faster. We performed mechanistic analyses of the temperature dependence of magnetic relaxation times considering Orbach relaxation processes, Raman-like relaxation and quantum tunnelling of magnetization (QTM). The effective energy barrier of the Orbach relaxation process (U_{eff}) is largest in compound **1** (19.2 cm^{-1}) and gradually decreases in the order **1** > **2** > **3** > **4** giving a minimum value in compound **4** (8.3 cm^{-1}), where the Raman-like mechanism showed the possibility of different types of phonon activity below and above ~2.5 K. As a precursor of **1**, the tetrahedral complex $[Co(H_2bip)Cl_2]$ (**1a**) was also synthesized and structurally and magnetically characterized: this compound exhibits slow relaxation of magnetization under an applied dc field (1800 Oe) with a record slow relaxation time of 3.39 s at 1.8 K.

Received 2nd May 2020,
Accepted 6th July 2021

DOI: 10.1039/d0dt01597k

rsc.li/dalton

Introduction

Mononuclear metal complexes represent the simplest, most tractable models to elucidate fundamental aspects of magnetic relaxation dynamics, important for the design of molecular magnets with enhanced properties. Systematic studies of mononuclear single molecule magnet (SMM)-type systems are important to provide a deeper understanding of magnetic anisotropy of the metal ions and coordination sphere influences on magnetic relaxation behaviour.

In the last few years, studies on magnetic properties of mononuclear 3d metal complexes have revealed that high-spin d^7 Co(II) is a promising candidate to exhibit slow relaxation of magnetization, intrinsic to SMM properties.[1,2] The high-spin Co(II) ion can exhibit a large range of magnetic anisotropy values with a flexible zero-field splitting parameter dependent on the coordination number and geometry. The coordination numbers of Co(II) SMMs range between two and eight.[3–10] Theoretical studies of such Co(II) complexes have established that conventional anisotropy considerations – negative axial (*D*) and negligible rhombic (*E*) parameters – are not essential criteria to obtain slow magnetic relaxation. In some cases, the field-dependent relaxation phenomenon in mononuclear Co(II) complexes with significant non-uniaxial anisotropy may be attributed to electronuclear spin entanglement.[9]

A $[Co^{II}(dmphen)_2(NCS)_2]$ compound was the first hexacoordinate Co(II) complex reported to exhibit slow relaxation of magnetization under an applied dc field of 1000 Oe, having positive axial and rhombic magnetic anisotropy parameters D = +98 cm^{-1} and E = +8.4 cm^{-1}, respectively.[10] Since then, several examples of hexacoordinate Co(II) complexes that exhibit SMM type behaviour have been reported.[4–8] Although there are several studies on the influences of geometrical parameters and/or short-range interactions, and theoretical supports, most of the reports focus on either single examples or comparisons between two complexes. Notably, systematic ana-

[a]*Department of Chemistry, Colorado State University, Fort Collins, CO 80523-1872, USA. E-mail: matthew.shores@colostate.edu*
[b]*Analytical Resources Core, Center for Materials and Molecular Analysis, Colorado State University, Fort Collins, Colorado 80523, USA*

† Electronic supplementary information (ESI) available. CCDC 1953030–1953032, 1953035 and 1999580. For ESI and crystallographic data in CIF or other electronic format see DOI: 10.1039/d0dt01597k

lyses of ligand modification on larger sets of structurally related complexes have not been investigated, as we attempt in this report.

In this work, we have envisaged a study of new hexa-coordinate Co(II) SMMs with a rational change of the ligand characteristics. The H_2bip ligand (2,2′-bi-1,4,5,6-tetrahydropyrimidine, Chart 1) is a bidentate chelating ligands widely used in our group for Fe(II) spin-crossover studies.[11–14] This ligand has been shown to significantly influence the properties of the metal centre depending on the first and second coordination environments, as well as supramolecular considerations.[12–14] Applied to Co(II), H_2bip should promote high spin (quartet) ground states.

We performed rational modifications of first and second coordination spheres of the metal centre, with the aim to correlate magnetic anisotropy changes to ligand set modification (Chart 1). A range of σ-donor (Cl > Br), π-donor (Br > Cl) and π-acceptor (bipyridine > imine) ligands can be incorporated into the complex while keeping two H_2bip ligands constant. The relative influence of spin–orbit coupling can be probed by comparison of the chlorido- and bromido-containing complexes, where according to the spectrochemical series the chlorido-generates a stronger σ-donor environment, while based on the nephelauxetic effect the bromido- is a stronger π-donor[15] and provides a larger contribution to the spin–orbit coupling, as described in some literature examples.[16,17]

Herein, we probe correlations between ligand field and dynamic magnetic properties in a family of Co(II) diimine compounds, comprising one tetracoordinate and four hexa-coordinate Co(II) complexes (Chart 1), all of which exhibit field-induced slow relaxation of magnetization.

Results and discussion

Syntheses and structures

Complexation of H_2bip to Co(II) ions is straightforward and rapid, owing to the lability of Co(II), but the isolation of pure compounds requires subtle adjustment of reactant and product solubilities *via* temperature, stoichiometry and solvent choice. We find that the chlorido-bound compound **1** is best made in two steps (Scheme 1), as the direct combination of 2 : 1 ratio of H_2bip : $CoCl_2$ in EtOH solution gives a mixture of crystalline compounds of different colours. In our hands, the most synthetically convenient route goes through the tetrahedral complex Co(H_2bip)Cl_2 (**1a**), which precipitates as a blue solid from EtOH. The blue-to-pink colour change upon dissolution in MeOH suggests the probable change of Co(II) coordination geometry from tetrahedral to octahedral through ligation by solvent molecules. The resulting species can serve as a precursor to **1** by addition of one more equivalent of H_2bip. Meanwhile, the Br-ligated analogue **2** can be made directly (Scheme 1): a combination of a 2 : 1 ratio of H_2bip : $CoBr_2$ gives a clean product *via* precipitation from EtOH at room temperature. If the reaction mixture containing additional H_2bip is heated, then the bromido ligands are displaced by H_2bip ligands to form the tris-H_2bip complex **3**. Like the Fe(II) analogue,[11–14] compound **2** serves as a precursor to heteroleptic Co(II) diimine complexes: addition of Me_2bpy to a solution of **2** in methanol also displaces bromido ligands to form the heteroleptic tris-diimine species **4**.

All four octahedral complex salts (**1–4**) crystallize in monoclinic crystal systems. X-ray parameters are listed in Table 4. In all four compounds (Fig. 1), two H_2bip ligands are *cis* oriented. The hexacoordinated Co(II) centres of compounds **1** and **2** have MN_4X_2 first coordination spheres, while compounds **3** and **4** show MN_6 first coordination spheres. All coordinated nitrogen atoms are sp^2 hybridized. In all four compounds, there are two crystallographically-distinct cobalt centres with small crystallographic differences. Table 1 contains the list of cobalt–ligand bond distances for **1–4**, showing that the average $Co–N_{H2bip}$ distances are comparable. We note that crystal structures of **1**, **2** and **3** show moderate to significant effects of twinning; where the crystal structure of **4** has significant solvent disorder; details are provided in the Experimental section. The Co–N distances are shorter for the H_2bip ligands than for the Me_2bpy ligands in the compound **4**.

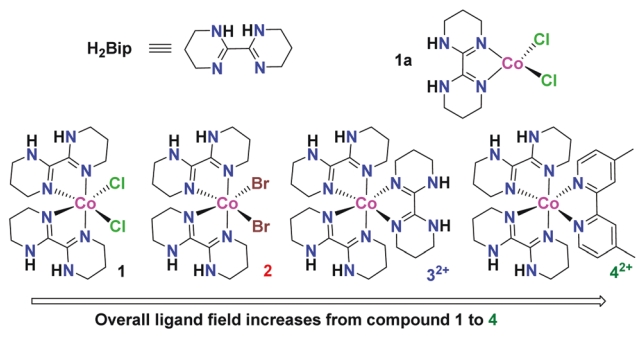

Chart 1 Schematic diagram of the rational change of ligand environment in the family of Co(II) complexes reported herein: successive substitution from a σ/π donor ligand chlorido (in **1**) to a π acceptor ligand 4,4′-Me-2,2′bpy (in **4**).

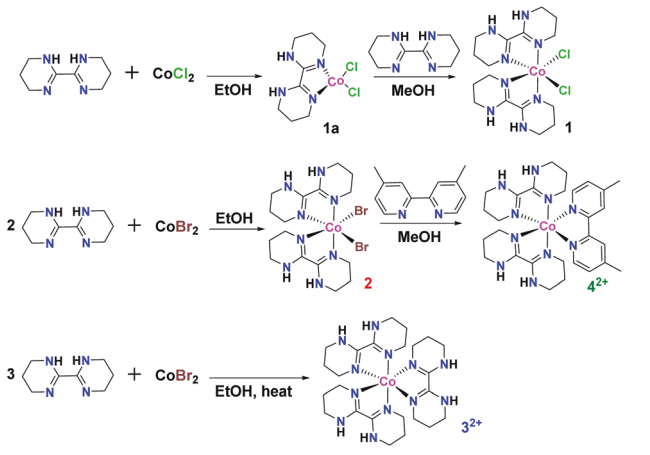

Scheme 1 Syntheses of Co(II) H_2bip complexes.

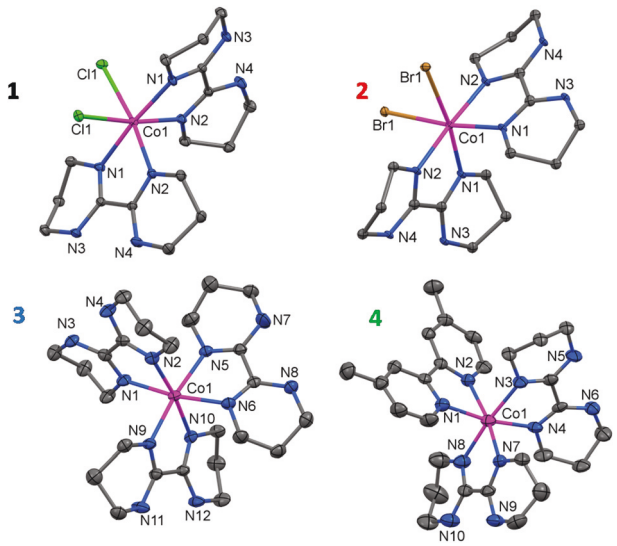

Fig. 1 Crystal structures of the Co-containing complexes in **1–4**, with thermal ellipsoids set at 50% probability level. Magenta, brown, green, blue and grey colours represent Co, Br, Cl, N, and C atoms, respectively. Hydrogen atoms, anions and solvents of crystallization are omitted for clarity.

Table 1 Selected bond distances (Å) in structures **1–4**

1		**2**	
Co1–N1	2.102(5)	Co1–N1	2.077(2)
Co1–N2	2.089(5)	Co1–N2	2.090(1)
Co1–Cl1	2.574(4)	Co1–Br1	2.718(5)
Co_2–N5	2.099(1)	Co_2–N5	2.069(1)
Co_2–N6	2.127(5)	Co_2–N6	2.112(2)
Co_2–Cl2	2.575(4)	Co_2–Br2	2.749(5)
3		**4**	
Co1–N1	2.099(4)	Co1–N1[a]	2.155(5)
Co1–N2	2.104(4)	Co1–N2[a]	2.151(6)
Co1–N5	2.120(4)	Co1–N3	2.118(6)
Co1–N6	2.147(4)	Co1–N4	2.098(5)
Co1–N9	2.101(4)	Co1–N7	2.102(6)
Co1–N10	2.114(4)	Co1–N8	2.097(6)
Co_2–N13	2.138(5)	Co_2–N11[a]	2.138(6)
Co_2–N14	2.120(5)	Co_2–N12[a]	2.158(6)
Co_2–N17	2.107(5)	Co_2–N13	2.137(6)
Co_2–N18	2.095(5)	Co_2–N14	2.106(6)
Co_2–N21	2.145(5)	Co_2–N17	2.084(6)
Co_2–N18	2.126(5)	Co_2–N18	2.110(6)

[a] Co–N distance to N atoms of Me_2bpy ligand.

Two non-coordinated bromides per Co(II) ion are found in the crystal packing of **3** and **4** to balance the cationic charges of those complexes. In **3**, additional MeOH solvate molecules (1 eq. per Co) are found in the crystal packing. In **4**, residual solvent molecules assigned as 4.5 eq. of acetonitrile molecules and one equivalent of water per unit cell are found as solvent of crystallization.

Intermolecular H-bonding interactions are observed in the crystal packing of all four compounds. The halido ligands of **1** and **2** interact with the amine (N–H) from the H_2bip ligands of neighbouring molecules (Fig. S2 and S3†). The closest separations of cobalt centres are comparable in **1** (8.200(1) Å) and **2** (8.059 Å). In the crystal packing of **3**, bromide anions, the H_2bip amine N–H and the O–H from MeOH molecules show extensive supramolecular interactions (Fig. S4†). In **3** the minimum cobalt–cobalt separation is 8.868(2) Å, which is ~0.67 Å longer than found in **1** and **2**. Similarly, hydrogen bonding is seen in the crystal packing of **4** (Fig. S5†) between the bromides and H_2bip N–H group; the water molecule in **4** also contributes in the hydrogen bonding with Br(3). Comparable to **3**, the minimum cobalt–cobalt separation in **4** is 8.846(1) Å.

The structure of the tetrahedral complex **1a** (Fig. 2 inset and S1†) shows Co(II) has a distorted tetrahedral geometry as coordinated by the imine nitrogen atoms of one H_2bip ligand and two chlorido ions. The $[Co(H_2bip)Cl_2]$ molecules form a pseudo-one-dimensional H-bonded chain along the *b* axis (Fig. S1(b)†) with close intermolecular contacts between the –N2–H2 of the H_2bip ligand and the Cl1 atoms of the neighbouring molecule. The H-bonding contact distance 3.214(2) Å (N2···Cl1) results in a Co···Co distance of 7.941(3) Å along the chain. These pseudo-chains are closely stacked, resulting in a shortest Co···Co distance of 5.784(3) Å between the chains (Fig. S1(b)†).

Static magnetic properties

Magnetic properties of the tetrahedral complex 1a. The temperature dependence of magnetic susceptibility for **1a** was recorded between 1.8–270 K under 1000 Oe dc applied field and the $\chi_M T$ *vs.* *T* data are shown in Fig. 2. At higher tempera-

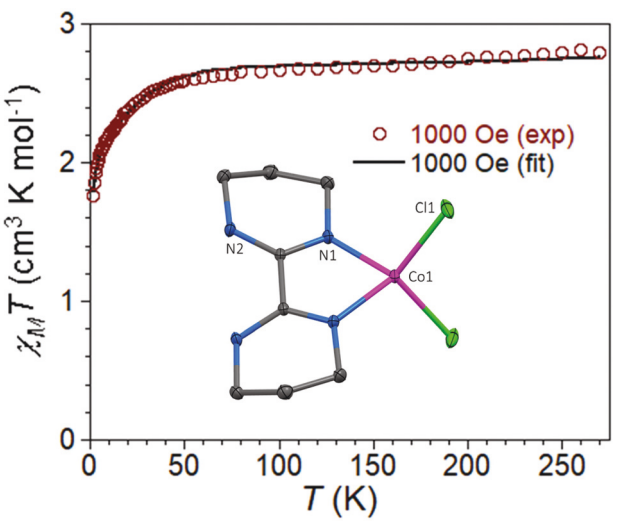

Fig. 2 Temperature dependence of $\chi_M T$ for **1a** under 1000 Oe dc field. The hollow circles represent the experimental data. The solid black line represents the fit to the data. Inset: crystal structure of the Co-containing complexes **1a**, with thermal ellipsoids set at 50% probability level. Magenta, green, blue and grey colours represent Co, Cl, N, and C atoms, respectively. Hydrogen atoms are omitted for clarity. The Co atom sits on a 2-fold rotation axis.

ture, the $\chi_M T$ value of **1a** (at 270 K) is 2.79 cm^3 K mol^{-1}, higher than the expected value of 1.875 cm^3 K mol^{-1} for an S = 3/2 system with g = 2; this high value is indeed the result of the orbital contribution typical for high spin Co^{II} metal complexes, there are several tetrahedral Co(II) SMMs that show comparable $\chi_M T$ values.[18–22] With decreasing temperature, the $\chi_M T$ product remains almost unchanged until 45 K, and then decreases further to 1.76 cm^3 K mol^{-1} at 1.8 K, indicating antiferromagnetic interactions and/or magnetic anisotropy in the system.

Fitting the $\chi_M T$ *vs.* T data with PHI,[23] the best fit gives parameters: $g_x = g_y$ = 2.11(6), g_z = 2.75(1), $|D|$ = 39.50 cm^{-1} and $|E|$ = 2.69 cm^{-1}, TIP = 6.67 × 10^{-4} emu mol^{-1}, and mean-field antiferromagnetic interaction zJ = −0.043 cm^{-1}. From this fit, the $|E/D|$ value is calculated as 0.068, which shows the axial nature of the magnetic anisotropy in compound **1a**. The H-bonding interactions and close packing of **1a** gave the shortest Co···Co distance of 5.784(3) Å, which justifies the presence of the antiferromagnetic interactions. We think the mean-field approximation is more appropriate over one dimensional (1D) model to estimate the antiferromagnetic interaction in this case because, there was no structural 1D chain through molecular bonding or coordination, and the pseudo-intra-chain Co···Co distance of 7.941(3) Å is longer than interchain Co···Co minimum distance of 5.784(3).

Magnetic properties of the octahedral complexes 1–4. Temperature dependencies of magnetic susceptibility data for compounds **1–4** are shown in Fig. 3. These data confirm quartet ground states for the Co(II) complexes and show comparable behaviour. Near room temperature, the corresponding $\chi_M T$ values of **1**, **2**, **3** and **4** are 3.39 (at 300 K), 3.37 (at 270 K), 2.87 (at 300 K), 2.93 (at 300 K) cm^3 K mol^{-1}, which are higher than the expected value of 1.875 cm^3 K mol^{-1} for an S = 3/2 spin with g = 2. Such high values of $\chi_M T$ are indeed the result of the orbital contribution typical for octahedral high-spin d^7 ions. With decreasing temperature, the $\chi_M T$ products remain relatively unchanged until around 100 K, and then gradually decrease to 2.35, 2.54, 1.61 and 1.85 cm^3 K mol^{-1} at 1.8 K for **1–4**, respectively, as a signature of the magnetic anisotropy found in these Co(II) complexes. In the crystal packing of the all four compounds, the cobalt–cobalt distances are comparable, ranging between 8.2–8.6 Å; thus, we expect the intermolecular antiferromagnetic interactions are similar in magnitude and not significant contributors to the magnetic behaviour.

The susceptibility data are fit in tandem with reduced field magnetization data, using PHI,[23] to spin Hamiltonians containing one magnetic centre which first provided us with $g_{x/y}$, g_z, axial anisotropy (D) and rhombic anisotropy (E) parameters for all four compounds (Table S1†). Relatively large magnitudes of axial (D) and large to small rhombic (E) anisotropy terms are found for all four compounds. For compounds **1** and **2**, the initial fits give negative D values and $|E/D|$ ratios larger than 1/3 (D = −66.68 cm^{-1} and E = 35.76 cm^{-1} for compound **1** (Fig. S34†); D = −72.62 cm^{-1} and E = 34.21 cm^{-1} for compound **2** (Fig. S36†)). Upon reorienting the D tensor (process in ESI†), we find large positive D values for **1** and **2** (Tables 2 and S1†).[25] Next we used these new D and E values of **1** and **2** to simulate the $\chi_M T$ *vs.* T and M *vs.* H/T data to determine the corresponding g_x, g_y, and g_z values as shown in Table 2 (Fig. S35 and S37†), which are in agreement with the positive axial anisotropy values found for **1** and **2**. To maintain a consistent data fitting protocol for all the compounds we simulated the $\chi_M T$ *vs.* T and M *vs.* H/T data of compounds **3** and **4** with their corresponding D and E parameters and determined the g_x, g_y, and g_z (Table 2).

Interestingly, the overall axiality (E/D) increases as we move to stronger field ligands, as exemplified in **4**. In contrast, the rhombic term does not show an obvious trend: we observe a large contribution in compounds **1** and **2** and a minimal presence in compounds **3** and **4**. There are distinct differences in the donor atom sets of compounds **1** and **2** (N_4X_2) in comparison to **3** and **4** (N_6), therefore the different electronics of the donor atom sets appear to influence the E/D ratio as well. From these results we surmise that increasing the σ-donor property facilitates large $|D|$. On the other hand, the π-acceptor property reduces the rhombic contribution significantly.

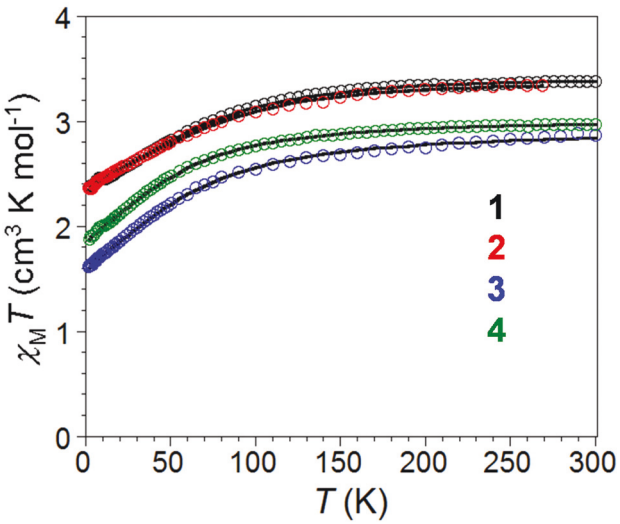

Fig. 3 Temperature dependence of $\chi_M T$ for **1–4**, collected at 1000 Oe dc field. The hollow circles represent the experimental data. The solid black lines are fits of the experimental data with PHI.

Table 2 Magnetic parameters derived from tandem fits to $\chi_M T$ *vs.* T and M *vs.* H/T data

	$g(x, y, z)$	D^a	$\lvert E\rvert^a$	$\lvert E/D\rvert$	R^2
1	2.09, 3.19, 2.66	+86.98[b]	15.46[b]	0.178[b]	99.9999
2	2.02, 3.20, 2.65	+87.63[b]	19.21[b]	0.219[b]	99.9998
3	2.54, 2.91[c]	−21.68	0.16	0.007	99.9307
4	1.88, 3.20, 2.22	+77.53	0.30	0.004	99.9999

[a] D and E values in cm^{-1}. [b] The D, E and $|E/D|$ values are recalculated using the rearrangement of the D_{xx}, D_{yy} and D_{zz} parameters according to ref. 25. Then rearrangement method is described in the ESI.† [c] Best fit was found using two g factors.

We note that the best fit for compound **3** provides a negative sign of D, which is distinct among the four octahedral complexes (Table 2). For compound **3** the simulation of the $\chi_M T$ *vs.* T and M *vs.* H/T data using fixed D and E gave poorer fits for three g factors (g_x, g_y, and g_z) than for two g factors ($g_{x/y}$ and g_z, Fig. S38†). We surmise that the local D_3 symmetry of **3** influences the nature and magnitude of its D parameter. Such change of local geometry (discussed in the AOM section of this manuscript) and the crystallographic environment influence the mixing of the ground and excited states, thus changes the sign and magnitude of D and E parameters. Note that, the magnitude of the $\chi_M T$ product of compound **3** is noticeably smaller than the other compounds, consistent with a lower degree of anisotropy. For perfect D_3 symmetry, the rhombic term E should be null for compound **3**. Like the others, **3** has two crystallographically distinct Co(II) centres, and the charge-balancing bromide anions and solvents of crystallization prevent exact three-fold symmetry in the lattice, enabling small but nonzero values of the E parameter. We note that the E value of compound **4** is also quite small (Table 2 and Fig. S39†), which is most probably due to the change in ligands resulting in a small magnetic excitation energy (discussed in the AOM section of this manuscript).

Attempts to fit only the M *vs.* H/T data with PHI[23] (Table S1†) and ANISOFIT[24] are in the ESI (Table S1 and Fig. S9, S40†): there, we find slightly different but comparable anisotropic parameters. The reproduction of the magnetization data using the spin-only Hamiltonian qualitatively depends on how isolated the ground state is from the excited states of Co(II).[25–29] In recent years several efforts have been made to construct improved Hamiltonians that consider magnetic functions beyond spin[26,27] to analyse the magnetic response of Co(II) complexes, especially using *ab initio* calculations.[28,29] In our current case, a theoretical analysis, and/or single crystal magnetization and/or EPR may shine more light to the in-depth analysis of anisotropic parameters, and will be considered in future collaborative works.

Dynamic magnetic properties

Alternating current (ac) magnetic susceptibility measurements were performed on crystalline samples of all compounds at temperatures between 1.8 K and 12 K. None of the compounds showed out-of-phase ac responses in zero applied field (Fig. S10–S13†), but all show slow relaxation of magnetization under relatively small applied dc fields (Fig. 4 and 5).

Dynamic magnetic properties of the tetrahedral compound 1a. At 3 K, **1a** exhibits slow relaxation of magnetization at applied 1000 Oe static field (Fig. S14 and S15†). The maxima of out-of-phase magnetic susceptibility (χ'') shift toward lower frequencies with an increase of applied dc field until 1800 Oe (Fig. S14†) and then start shifting toward higher frequencies until 2200 Oe. Interestingly, with the further increase of dc field beyond 2500 Oe, we see an increase of the χ'' magnitude until 8000 Oe along with shifts toward lower frequency (Fig. S15†). We assume that the applied field above 2500 Oe (Fig. S15†) decouples some intermolecular Co(II)–Co(II) interactions and further slows down the magnetic relaxation. Within our measurement range (0.05–1488 Hz), the magnitude of $\chi''(\nu)$ increases until 8000 Oe and the relaxation time is longest at 8000 Oe (3 K) (Fig. S15†). Note that this type of field dependence of the relaxation time can be further studied for quantum dynamics of molecular qubits, but is outside the scope of current work.[30,31] We selected the dc field corresponding to the first minimum of relaxation time ($\chi''(\nu^{max})$), (Fig. S16†), 1800 Oe, to perform further studies on the temperature and frequency dependence of χ''. The temperature and frequency dependence of χ' and χ'' at 1800 Oe show slow relaxation of magnetization below 3.25 K (Fig. 4). The relaxation time (τ) of **1a** is deduced as a function of the temperature ($\tau(T) = 1/(2\pi\nu)$) from the maximum of $\chi''(\nu)$ curves between 1.8–3.25 K and fitted with the Arrhenius law: $\tau(T) = \tau_0 \exp(U_{eff}/k_B T)$, giving $U_{eff} = 4.82$ cm^{-1} (6.06 K) and $\tau_0 = 0.113$ s, where τ_0 is the pre-exponential constant and U_{eff} is the energy needed to reverse the magnetization according to the Orbach relaxation process (Fig. 4 inset).

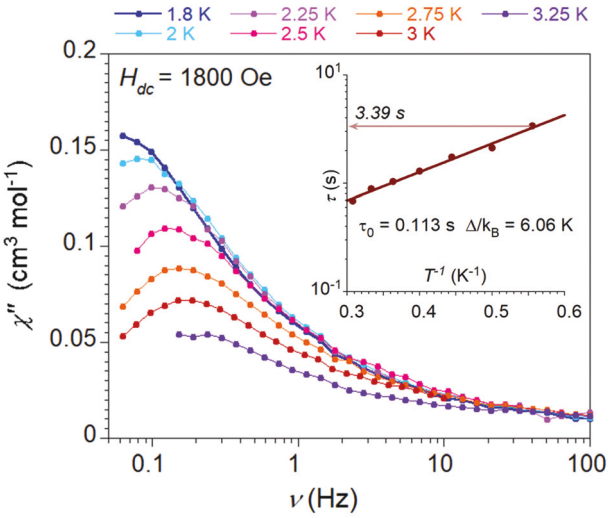

Fig. 4 The frequency dependence of the imaginary part of the ac magnetic susceptibility (χ'') for compound **1a** at an applied dc field of 1800 Oe and 4 Oe oscillating ac field at different temperatures between 1.8 K and 3.25 K. Inset: semilog plot of $\tau(T)$ *vs.* T^{-1} for **1a** and fit to $\tau(T) = \tau_0 \exp(U_{eff}/k_B T)$: the relaxation time at 1.8 K is as slow as 3.4 s.

Because of the small U_{eff} and high τ_0 values, we have considered alternative relaxation processes in **1a**, including Raman and phonon bottleneck mechanisms. The fit of the τ^{-1} *vs.* T data with power-law $\tau^{-1} = bT^n$ provides the polynomial exponent $n = 2.54$ with matrix coefficient $b = 0.073$ (Fig. S32†). The value of $n \approx 2$ indicates the possible presence of a phonon bottleneck mechanism. Addition of a Raman or direct relaxation pathways to the phonon bottleneck with $n = 2$ restriction does not provide good data fitting parameters. Note that **1a** has a magnetic relaxation time as slow as 3.39 s at 1.8 K (Fig. 4 inset), which to our knowledge is the slowest relaxation time recorded for a Co(II) field-induced spin–lattice relaxation. In reported literature records, a hexacoordinate Co(II) SMM [Co

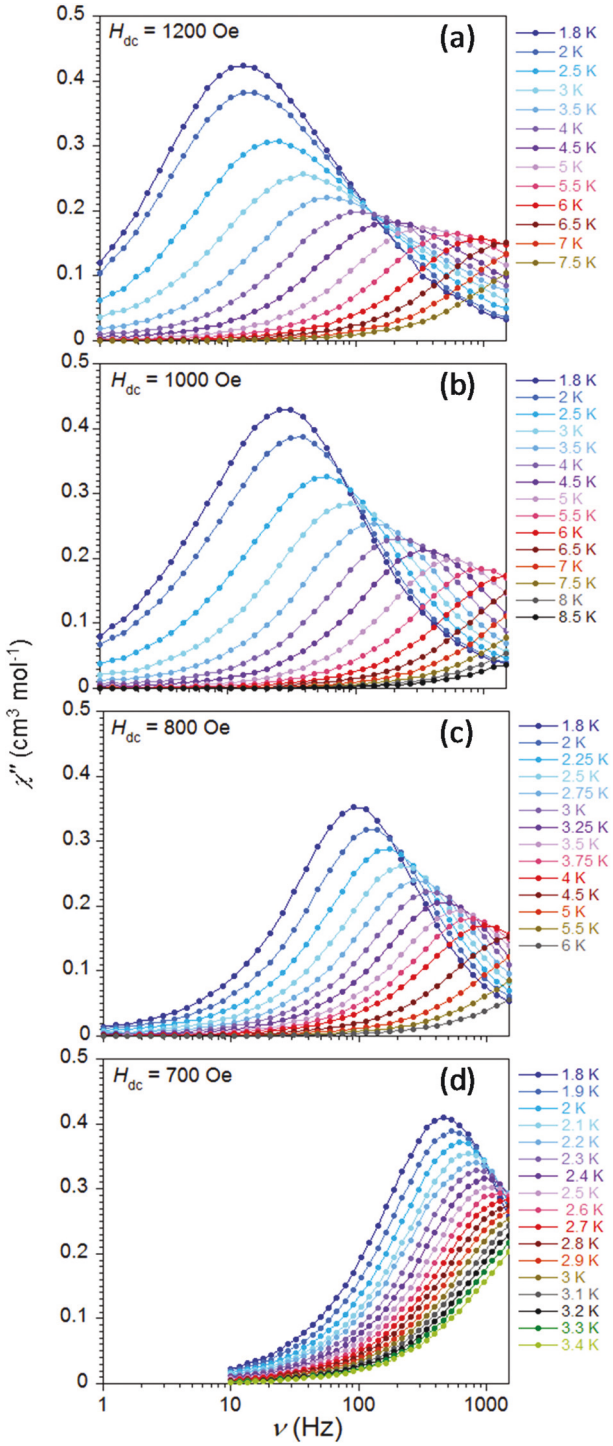

Fig. 5 Frequency and temperature dependence of the imaginary part of the ac magnetic susceptibility (χ'') for **1** (a), **2** (b), **3** (c) and **4** (d), at applied dc fields and 4 Oe oscillating ac field.

(pydca)(dmpy)]$_2$·H_2O pydca = pyridine-2,6-dicarboxylato, dmpy = 2,6-dimethanolpyridine shows a relaxation time of 1.35 s at T = 1.9 K and applied field of 4000 Oe.[32]

Dynamic magnetic properties of the octahedral compounds 1–4. Slow relaxation dynamics of magnetization emerge for compound **1** above an applied dc field of 200 Oe (at 2.5 K, Fig. S17†), where the maxima χ'' shift toward lower frequencies with an increase of applied dc field until 1200 Oe. With further increase of applied dc field after 1200 Oe, the maxima of the χ'' again move toward the higher frequencies, which implies that compound **1** relaxes most slowly near 1200 Oe (Fig. S18†). Therefore, the temperature and frequency dependence of both in-phase and out-of-phase magnetic susceptibilities were collected for **1** at 1200 Oe (Fig. 5a and S19, S20†). Slow magnetic dynamics in **1** are observed below 8 K (Fig. S19†), the relaxation time (τ) of **1** is deduced as a function of the temperature ($\tau(T) = 1/(2\pi\nu)$) from the maxima of $\chi''(\nu)$ curves obtained at different temperatures (Fig. 5a and S20†).

Compound **2** exhibits a maximum magnitude of out-of-phase relaxation at 1000 Oe dc field, as measured at 4 K (Fig. S21†). At this field, compound **2** shows slow relaxation of magnetization below 7 K (Fig. S22†). The frequency dependence of the in-phase (χ') part and out of phase (χ'') part of the ac magnetic susceptibility are shown in Fig. 5b and S23,† respectively. Notably, compared to compound **1**, the frequency dependence profile for **2** shifts towards the higher frequency regime, indicating faster relaxation of magnetization; relaxation times $\tau(T)$ at 1.8 K are provided in Table 3. Similarly, the required dc fields to obtain the maximum out of phase magnetic susceptibility response are 800 Oe (at 3 K) and 700 Oe (at 1.8 K) for compounds **3** and **4**, respectively (Fig. S24 and S27†). At those applied dc fields, **3** and **4** exhibit magnetic relaxation below 5.5 K and 4 K, respectively (Fig. S25 and S28†). The frequency dependence of the in-phase (χ') and out of phase (χ'') parts of the ac magnetic susceptibility are shown in Fig. 5c and d, S26 and S29.† Relaxation times $\tau(T)$ are maximized for **3** and **4** at the same temperature (1.8 K) and decrease by an order of magnitude between **3** and **4** (Table 3). Notable here, as the overall ligand field strength successively increases, the required field for maximum response decreases, and the relaxation time also decreases monotonically.

The temperature-dependent relaxation times $\tau(T)$ for compounds **1–4** are derived from the maxima of $\chi''(\nu)$ curves at different temperatures (Fig. 5). The temperature dependence of these values can be fit to an Arrhenius expression, $\tau(T) = \tau_0 \exp(U_{eff}/k_BT)$, to give barriers ($U_{eff}$) and relaxation times for Orbach relaxation (Fig. S31† and Table 3). The linear part of the log plot of $\tau(T)$ *vs.* $1/T$ (Fig. S31†) for compounds **1–4**,

Table 3 Magnetic relaxation parameters for compounds **1–4** with Orbach-like or Raman-like mechanism above ~2.5 K

Parameter	**1**	**2**	**3**	**4**
H_{dc} (Oe)	1200	1000	800	700
τ (1.8 K) in s	1.3×10^{-2}	6.2×10^{-3}	1.7×10^{-3}	3.4×10^{-4}
U_{eff} [a] (cm^{-1})	19.2	16.0	8.9	8.3
τ_0 [a] (s)	1.67×10^{-6}	2.45×10^{-6}	6.47×10^{-6}	1.27×10^{-6}
b [b] (s^{-1} K^{-n})	1.82	6.23	51.93	221.41
n [b]	4.45	4.00	3.44	3.75

[a] $\tau(T) = \tau_0 \exp(U_{eff}/k_BT)$, Fig. S31.† [b] $-\ln(\tau) = \ln b + n \ln(T)$, $b = \exp(\ln b)$, Fig. S42.†

respectively, finds U_{eff} = 19.2, 16.0, 8.9 and 8.3 cm^{-1}, where the preexponential constant τ_0 ranges between 1.67 × 10^{-6} s and 1.27 × 10^{-6} s (Table 3), but this method does not reproduce the low-temperature data very well.

The Cole–Cole plots of $\chi'(\nu)$ *vs.* $\chi''(\nu)$, fit to the generalised Debye model for a single relaxation pathway (Fig. S30†), give a distribution of relaxation times (α parameter range), strongly suggesting that Orbach like relaxation does not fully describe the behaviour. Compounds **1** and **2** show large ranges of α parameters, indicating the wider distribution of relaxation times compared to compounds **3** and **4**. The α parameter ranges between 0.238–0.027 (for **1**), 0.174–0.013 (for **2**), 0.052–0.016 (for **3**) and 0.044–0.008 (for **4**). As the slope of the $\tau(T)$ *vs.* $1/T$ data (Fig. S31†) decreases at low temperatures (below ~2.5 K) we considered the presence of quantum tunnelling of magnetization (QTM) at a low-temperature regime. We fit the data with a combination of QTM and Orbach relaxation mechanisms using the relation $\tau(T)^{-1} = \tau_{QTM}{}^{-1} + \tau_0{}^{-1} \exp(U_{eff}/k_BT)$, where the τ_{QTM} is relaxation time of QTM (Fig. 6 and Table S2†). As expected, the fitting parameter shows that the magnitudes of τ_{QTM} and U_{eff} are highest in **1** and smallest in **4** with the trend **1** > **2** > **3** > **4**, as shown in Table S2.† These derived values of U_{eff} with or without QTM are almost one order of magnitude lower than the theoretical values of the energy gap between the ground and the excited Kramers doublet states, $U_{theo} = 2(D^2 + 3E^2)^{1/2}$, which is frequently observed in hexacoordinate Co(II) SMMs.[6–8,33] Interestingly, as we have found for the E/D values of '**1** and **2**' *vs.* '**3** and **4**' showed a similarity within the pair of N_4X_2 *vs.* N_6 coordination (Table 2), likewise in Table 3 the U_{eff} values of **1** and **2** are comparable (near 20 cm^{-1}) where the U_{eff} values of **3** and **4** are comparable (near 10 cm^{-1}). Notwithstanding, we note that, although the addition of QTM improves the fit, the data below 2.5 K (greyed region in Fig. 6) are still not in good agreement with the model.

We have also fit the $\tau(T)^{-1}$ *vs.* T data to a Raman relaxation process (Fig. 6 and Fig. S33†) with the equation $\tau^{-1} = bT^n$; results are collected in Table S2.† The addition of a direct relaxation process to any of the above-mentioned mechanisms does not provide reasonable fitting parameters. The fit of the τ^{-1} *vs.* T data with power-law $\tau^{-1} = bT^n$ provides the polynomial exponent n = 5.45, 4.85, 3.46, and 2.90 respectively for compounds **1** to **4** (see Table S2†). We find both Orbach + QTM and Raman-like models reproduce the high-temperature data pretty well above 3 K but the low-temperature data below 2.5 K (greyed region in Fig. 6 and 7) do not agree well with any of these models. For the compounds with positive anisotropy (**1**, **2** and **4**) the physical meaning of QTM involving the spin states is not so practical, therefore we have considered fitting the $\ln(\tau)$ *vs.* $\ln(T)$ data (Fig. 7 (left)) separately at low and high temperatures using Raman-like relaxation. In the low-temperature regime of the linear $\ln(\tau)$ *vs.* $\ln(T)$ fit (the solid straight line, Fig. 7 (right), S41†) we find that the fit lines are mostly parallel to each other with comparable slope (n), given n = 2.28, 2.53, 2.60, and 2.52 (Table S2†) respectively for compounds **1** to **4**. This may indicate that the same types of phonons are driving the spin–lattice relaxation in all four systems at low temperatures (below ~2.5 K). At temperatures above 2.5 K, linear fits of $\ln(\tau)$ *vs.* $\ln(T)$ data (the solid straight lines) show that the slopes differ for all the compounds, giving n = 4.45, 4.00, 3.44 and 3.75 (see Fig. 7 (right), S42 and Table S2†), respectively, for compounds **1** to **4**. Therefore, we can conclude that the high-temperature magnetic dynamics are influenced by the local coordination and/or extended geometry of the Co(II) complexes.

For a Kramer ion like Co(II) with S = 3/2, it theoretically follows a power-law dependence of temperature, $\tau^{-1} = bT^9$. But, in practice, the eigenstates of the optical and acoustic phonon in the lattices can interact with the spin and the n term can be much lower[34–37] and also different types of phonons may play roles in the spin–lattice relaxation. Note that in current cases, the H *vs.* ν^{max} plots of these compounds (Fig. S18, S21, S24 and S27†) show significant field and frequency dependence of

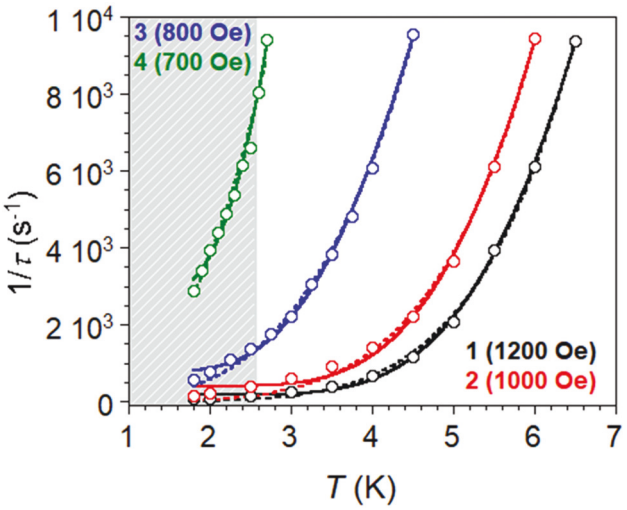

Fig. 6 Temperature dependence of relaxation times for **1–4**. Solid lines are best fits to the relation $\tau(T)^{-1} = \tau_{QTM}{}^{-1} + \tau_0{}^{-1} \exp(-U_{eff}/k_BT)$, a combination of Orbach and QTM relaxation mechanisms. The dotted lines are the best fits to the relation $\tau(T)^{-1} = bT^n$ for the Raman relaxation mechanism. Both models reproduce the high-temperature data, but the low-temperature data below 2.5 K (greyed region) are not in good agreement with any of the models.

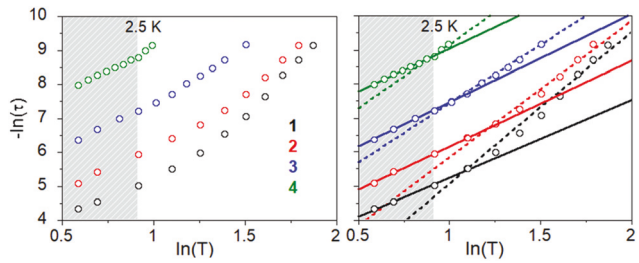

Fig. 7 (Left) The $\ln(\tau)$ *vs.* $\ln(T)$ plots of experimental data. (Right) Linear fits of the $\ln(\tau)$ *vs.* $\ln(T)$ data with two types of Raman relaxation mechanisms: solid lines for low-temperature regime (greyed regime, below ~2.5 K) and dotted lines for the higher-temperature regime.

the χ'' data. Although the field dependence of the Raman relaxation is known for some systems like V(IV),[34,35] Mn(IV)[36] and Ni(III),[37] in those cases, the field dependent χ'' (max) response usually moves to lower frequency as the applied dc field increases until above 1 T or higher. In contrast, for compounds **1–4** the χ'' (max) response maximizes between 700–1200 Oe, which is much lower than 1 T. The *H vs.* ν^{max} relation for the current Co(II) complexes shows that, above a certain field (much lower than 1 T), χ'' (max) moves to a higher frequency, corresponding to a faster spin–lattice relaxation. Therefore from the magnetic dynamic analysis shown in Fig. 6 and 7, we hypothesize that at low temperatures the slow magnetic relaxation is a phonon driven Raman-like relaxation, but at high temperature (above ~2.5 K), it could be a varied power-law (Raman-like) or exponential (Orbach-like) mechanism or a mixture of both. Regardless of what relaxation mechanism(s) are operative, we see that the trend holds where '**1** and **2**' *vs.* '**3** and **4**' showed a similarity within the pair of N_4X_2 *vs.* N_6 coordination. So, it is safe to assume that replacing the Cl atoms of compound **1** with more σ-donor type ligands may slow down the magnetic relaxation dynamics.

In some recent literature studies, systematic approaches have been adopted to explore correlations between donor/acceptor ligand properties and magnetic anisotropy and/or U_{eff} values of hexacoordinated Co(II) SMMs.[6–8] An octahedral Co(II) SMM system bearing Co–S/Se axial coordination exhibits lower relaxation time and U_{eff} values for the Se-containing complex, which is attributed to the orbital effect of heavier donor atom Se.[8] A change of coordinated pseudohalides (NCS, NCSe, $N(CN)_2$) on a different Co(II) complex also showed trends in the magnetic anisotropy as $D(NCSe^-) > D(NCS^-) > D(N(CN)_2^-)$.[8] The relaxation dynamics showed one relaxation mode for NCS- and NCSe-containing compounds at 1000 Oe but two modes at 6000 Oe, whereas $N(CN)_2$ showed only one relaxation process.[8]

Our systematic analysis of compounds **1–4** suggests a strategy to manipulate the magnetic dynamics of hexacoordinate Co(II) SMMs. From the monotonic decrease of U_{eff} and relaxation times from compounds **1–4** we hypothesize that reducing the overall ligand field of hexacoordinate Co(II) ions may lead to SMMs with longer relaxation times.

Angular overlap model (AOM) analysis

Toward elucidating deeper correlations of the magnetic properties of hexacoordinate Co(II) SMMs with their first coordination spheres, we applied the qualitative approach of angular overlap model (AOM)[21,38–44] to compounds **1–4**. The AOM is a simple tool to interpret the d orbital splitting of 3d metal complexes. Our aim in applying AOM is to investigate how the d orbital energies of compounds **1–4** are changing with ligand e_σ and e_π values and explore relative orbital energy contributions to anisotropy and magnetic relaxation. Although AOM gives approximate energies,[45] and several advanced theoretical methods are able to demonstrate more precise energy levels,[46] the AOM model offers experimentalists a simplified and rapid understanding of ligand field effects that may lead us to predict the design of similar Co(II) SMMs with enhanced relaxation times.

As a model (Fig. 8, see ESI† for detail), we placed the halides along the *x* and *y* directions for **1** and **2**, which are substituted by H_2bip and Me_2bpy for **3** and **4**, respectively. Since the AOM parameters of the ligands we used in this work are not available in the literature, we chose approximate e_σ and e_π values for our ligands on the basis of literature studies.[38–45,47] The e_π values successively decrease from compound **1** to **4**, but the order of e_σ values have a different trend: e_σ (Br) < e_σ (Cl) < e_σ (N_{imine}) < e_σ (N_{bipy}). The bromido ligand is a weaker σ donor than chlorido, raising d_{z^2} and $d_{x^2-y^2}$ of Cl-containing **1** relative to Br-containing **2**, but the d_{xy}, d_{xz} and d_{yz} orbitals of **1** are also higher in energy than for **2**. Because of the simplified point charge assumption of the AOM model, compound **3** has a perfect octahedral splitting despite the molecular D_3 symmetry. For compounds **1** and **2** the d_{z^2} orbitals are highest in energy. In contrast, for compound **4**, due to the negative e_π value, $d_{x^2-y^2}$ becomes the most destabilized orbital and d_{xy} the most stabilized.

Electronic absorption data collected in MeOH (Fig. S6†) support in part the energy gaps computed *via* AOM. Although metal–ligand charge transfer (MLCT) and instrument limitations preclude direct observation of d–d bands, maxima in the visible spectrum show MLCTs increasing from compound **1** (512 nm) to **4** (488 nm). The AOM-predicted d–d transitions (Fig. 8) from the $^4T_1$ to $^4T_2$ states are much lower in energy, ranging from 8850 cm^{-1} (1129 nm) in **1**, to 8400 cm^{-1} (1190 nm) in **2**, to 10 100 cm^{-1} (990 nm) in **3**, and 11 200 cm^{-1} (891 nm) in **4**. The parallel increase of observed MLCT and computed d–d transitions in compounds **1** to **4** infers shifting of "e_g" orbitals toward higher energy in **4**.

The AOM results show that the increased energy gap between the ($d_{x^2-y^2}$/d_{z^2}) and (d_{xy}/d_{xz}/d_{yz}) sets correlates with the decrease of axiality ($|E/D|$) of the magnetic anisotropy, where **1** and **2** have large $|E/D|$ values and **4** has the smallest. We find a similar trend in the relaxation times ($\tau(s)$) and effective energy

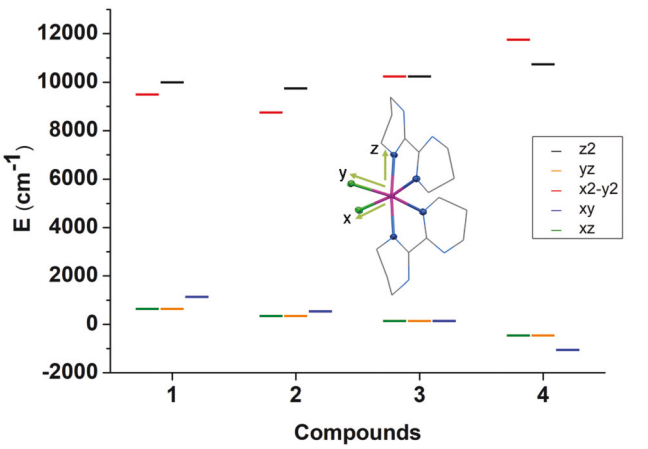

Fig. 8 Schematic representation of the energy levels of 3d orbitals of Co(II) for compounds **1–4** on the basis of angular overlap model (AOM).

barriers for magnetic relaxation (U_{eff}) (Tables 2 and 3). Based on this correlation, we hypothesize that substituting the chlorido/bromido with ligands possessing larger e_σ and e_π (*e.g.* fluorido, hydroxido) will generate Co(II) SMM systems with higher U_{eff} and relaxation times, whereas substitution with stronger π acceptor ligands will decrease the U_{eff} and relaxation times.

Studies of first-row transition metal complexes with various coordination modes have shown that the magnitude of D depends on the degree of distortion induced by the Jahn–Teller effect.[48,49] The first excitation energy involves the nonbonding and the antibonding d orbitals, which are also involved in Jahn–Teller distortion. Depending on which orbitals are involved in the magnetic excitations, the magnitude and sign of D and E values may change.[49] The D and E parameters are calculated based on the diagonalized D tensors: $D = D_{zz} - (D_{xx} + D_{yy})/2$ and $E = (D_{xx} - D_{yy})/2$, where the values of D_{ii} depends on the excitation energies: larger excitation energies result in smaller D_{ii} values.[22,48,49] From AOM we find d_{xy} is changing relative to d_{xz}/d_{yz}. For compounds **1** and **2**, the possible excitation involves d_{xz}/d_{yz} ($m_l = \pm1$) and $d_{x^2-y^2}$ ($m_l = \pm2$) orbitals: the π-donor property of the halido ligands may destabilize low lying d_{xz}/d_{yz} and contribute to the large D.[48] The contribution of the both nonbonding (d_{xz}/d_{yz}) and antibonding ($d_{x^2-y^2}$) orbitals results in large E in **1** and **2**, as the values of D_{xx} and D_{yy} are significantly different. In compound **4** the d_{xy} is the lowest-lying orbital, where the d_{xz}/d_{yz} (stabilized by π acceptor ligand) orbitals further split due to Jahn–Teller distortion and contributes to the first excitation involving $|m_l| = 1$. The smaller d_{xz} to d_{yz} excitation energy results in larger positive D, where comparable D_{xx}/D_{yy} attributes to small E. The degeneracy of the nonbonding d orbitals of compound **3** should be affected by Jahn–Teller-induced geometrical distortion (not shown in Fig. 8), although that distortion may not be large. From the smaller magnitude of the D and E of **3** (Table 2) we can speculate that both nonbonding d_{xz}/d_{yz} ($m_l = \pm1$) and d_{z^2} ($m_l = 0$) orbitals may participate in the excitation. The e_π of di-imine is much smaller than halido, but larger than bipyridine ligands, therefore d_{xz}/d_{yz} are not as destabilized as **1** and **2**, thus have higher excitation energy and lower D value.[48]

Overall, our discussion of the anisotropic value distribution of Table 2 and the AOM estimation indicates that a more axial anisotropy (D) could be achievable by employing ligands possessing large e_π values (*e.g.* fluorido, hydroxido).

Conclusions

We have performed a systematic study of ligand field influences on dynamic magnetic properties of hexa-coordinate Co(II) diimine complexes. We find in this set of compounds interesting trends in magnetic anisotropy, relaxation time and U_{eff}, where larger e_σ and e_π increase magnetic relaxation times. As there are few examples of a *series* of Co(II) SMMs studied in the light of rational ligand modification, these results will contribute to efforts to tune magnetic anisotropy and/or relaxation in mononuclear paramagnetic complexes. From a simple AOM model we can predict that using stronger π-donor ligands may lower the energy gap between $d_{x^2-y^2}$ and d_{z^2} orbitals and d_{xy}, d_{xz}, and d_{yz} set, which offers a straightforward approach to improve the magnetic dynamic properties of these types of Co(II) SMMs. Our future studies in this system include the replacement of the chlorido/bromido with weaker σ donors, and systematic probing of supramolecular effects on magnetic relaxation through intermolecular interactions *via* NH moieties on the H_2bip ligands. In addition, we expect that more elaborate ac magnetic measurements at various fields and frequencies may further differentiate relative contributions of different relaxation mechanisms like Orbach, Raman, phonon bottleneck and quantum tunnelling of magnetization.

Experimental section

Preparation of compounds

Unless otherwise noted, compound syntheses and manipulations were performed inside a dinitrogen-filled glovebox (MBRAUN Labmaster 130). The preparation of H_2bip (= 2,2′-bi-1,4,5,6-tetrahydropyrimidine) has been described elsewhere.[50] Anhydrous methanol (MeOH) and ethanol (EtOH) were purchased from Sigma Aldrich as Sure/Seal bottles. Other solvents were sparged with dinitrogen, passed over molecular sieves, and degassed prior to use. The 4,4′-methyl-2,2′-dipyridyl (Me_2bpy) ligand was supplied by Reilly Tar & Chemical Corporation site, Indianapolis, Indiana and recrystallized from ethyl acetate.[51] All other reagents were obtained from commercial sources and were used without further purification.

$Co^{II}(H_2bip)Cl_2$ (1a). Solid $CoCl_2$ (65 mg, 0.5 mmol) was dissolved in 10 mL of EtOH with warming near 50 °C. To this was added a 4 mL EtOH solution containing 83 mg (0.5 mmol) of H_2bip, resulting in the immediate precipitation of a blue solid that was collected by filtration. The blue precipitate was dissolved in MeOH to give a pink-coloured solution. Diffusion of diethyl ether vapour into this solution over 2 days afforded blue rod-shaped crystals suitable for single-crystal X-ray diffraction. The product (121 mg, yield 81%) were collected by filtration. IR (ATR): $\nu_{C=N}$ 1618, 1582 cm^{-1}. Elemental analysis of **1a** calculated (%) for $C_8H_{14}Cl_2CoN_4$ (formula weight (FW) = 296.06 g mol^{-1}): C 32.45, H 4.77, N 18.92; and experimentally found (%) as C 32.33, H 4.59, N 19.05.

$[Co^{II}(H_2bip)_2Cl_2]$ (1). A solution of H_2bip (17 mg, 0.1 mmol) in 1 mL of MeOH was added to a solution of **1a** (30 mg, 0.1 mmol) in 2 mL of MeOH. Diethyl ether vapour diffusion into the solution over two days afforded 37 mg (yield 80%) of pink block crystals of **1** suitable for single crystal X-ray diffraction studies. Note that if the diffision is allowed go longer that 2–3 days, some green microcrystals appear on the top layer of crystalization. IR (ATR): $\nu_{C=N}$ 1610, 1582 cm^{-1}. Elemental analysis of **1** calculated (%) for $C_{16}H_{28}Cl_2CoN_8$ (FW = 462.29 g mol^{-1}): C 41.57, H 6.10, N 24.24; and experimentally found (%) as C 41.63, H 5.99, N 24.15.

$[Co^{II}(H_2bip)_2Br_2]$ (2). A solution of H_2bip (67 mg, 0.4 mmol) in 4 mL of EtOH was added to a stirring solution of $CoBr_2$

(44 mg, 0.2 mmol) in 10 mL of EtOH. After approximately 30 minutes, a pink precipitate formed; the mixture was stirred for an additional two hours. The precipitate was collected by filtration and recrystallized *via* diethyl ether vapour diffusion into a methanolic solution of the crude product. After 2 days, pink block crystals of **2** suitable for single-crystal X-ray analysis were collected by filtration, to afford 86 mg (yield 77%) of product. IR (ATR): $\nu_{C=N}$ 1614, 1590 cm^{-1}. Elemental analysis of **2** calculated (%) for $C_{16}H_{28}Br_2CoN_8$ (FW = 551.19 g mol^{-1}): C 34.86, H 5.12, N 20.33. Found: C 34.98, H 5.04, N 20.48.

$[Co^{II}(H_2bip)_3]Br_2\cdot(MeOH)_1$ (3). A solution of H_2bip (100 mg, 0.6 mmol) in 4 mL of EtOH was added to a solution of $CoBr_2$ (44 mg, 0.2 mmol) dissolved in 10 mL of EtOH with warming, to result in an orange solution. This was stirred for two additional hours at 50 °C. The solution was cooled to room temperature and evaporated to dryness and the residue was re-dissolved in 4 mL of MeOH. Diffusion of diethyl ether vapour through the solution over 2 days afforded 105 mg (yield 70%) of orange needle-shaped crystals of **3** suitable for single crystal X-ray diffraction analysis. The single crystal X-ray structure is consistent with the presence of one MeOH per Co(II) ions. IR (ATR): $\nu_{C=N}$ 1609, 1571 cm^{-1}. Elemental analysis of **3** calculated (%) for $C_{25}H_{46}Br_2CoN_{12}O$ (FW = 749.45 g mol^{-1}): C 40.09, H 6.12, N 22.44; and experimentally found (%) as C 40.11, H 6.06, N 22.49.

$[Co^{II}(H_2bip)_2(Me_2bpy)]Br_2$ (+solvent) (4). A solution of Me_2bpy (18 mg, 0.1 mmol) in 2 mL of MeOH was added to a solution of (**2**) (55 mg, 0.1 mmol) in 3 mL of MeOH to afford an orange solution. The solution was stirred for 2 hours and then evaporated to dryness. The orange residue was re-dissolved in 3 mL of acetonitrile. Diffusion of diethyl ether vapour to the solution yielded 54 mg (yield 71% based on compound **2**) of X-ray quality orange needle-shaped crystals after 4 days. The single crystal X-ray structure is consistent with the presence of 0.5 MeCN molecule and 0.25 water per Co(II) ion. Although all the reacion was done in glove box, we guess that the water molecule may come from the ligand (Me_2bpy) or the acetonitrile. IR (ATR): $\nu_{C=N}$ 1611, 1581 cm^{-1}. Elemental analysis of **4** calculated (%) for $C_{29}H_{42}Br_2CoN_{10.5}O_{0.25}$ (FW = 760.45 g mol^{-1}): C 45.80, H 5.57, N 19.34; and experimentally found (%) as C 46.01, H 5.50, N 19.49.

X-ray structure determinations

Crystals suitable for X-ray analysis were coated with paratone–N oil and supported on a Cryoloop before being mounted on a Bruker D8 Kappa ApexII CCD diffractometer under a stream of dinitrogen. Data collection was performed at 120(1) K using an Oxford 700 cryo-system with Mo-Kα radiation (λ = 0.71073 Å) and a graphite monochromator, targeting complete coverage and 4-fold redundancy.[52] Crystallographic data and metric parameters are presented in Table 4. Determination of unit cell parameters through refinement, data collection, reduction, and correction for Lorentz and polarization effects for were performed using the SAINT software package.[53] Data were sorted, scaled, averaged, and corrected for semiempirical absorption affects with SADABS.[52–54] The structures were solved with the ShelXT structure solution program and refined with the ShelXL-2017 refinement packakge.[55,56] Unless otherwise noted, thermal parameters for all non-hydrogen atoms were refined anisotropically. Hydrogen atoms were added at calculated positions and were refined using a riding model.

Table 4 Single crystal X-ray diffraction parameters for all compounds

	$[Co(H_2bip)Cl_2]$ (**1a**)	$[Co(H_2bip)_2Cl_2]$ (**1**)	$[Co(H_2bip)_2Br_2]$ (**2**)	$[Co(H_2bip)_3](Br)_2\cdot(MeOH)$ (**3**)	$[Co(H_2bip)_2(Me_2bpy)](Br)_2\cdot(MeCN)_{0.5}\cdot(H_2O)_{0.25}$ (**4**)
CCDC number	1953030	1953031	1999580	1953032	1953035
Empirical formula	$C_8H_{14}Cl_2CoN_4$	$C_{16}H_{28}Cl_2CoN_8$	$C_{16}H_{28}Br_2CoN_8$	$C_{100}H_{180}Br_8Co_4N_{48}O_4$	$C_{116}H_{162}Br_8Co_4N_{42}O$
FW (g mol^{-1})	296.06	462.29	551.21	2993.91	3035.87
Temperature (K)	120	120	120	120	120
Wavelength (Å)	0.71073	0.71073	0.71073	0.71073	0.71073
Crystal system	Monoclinic	Monoclinic	Monoclinic	Monoclinic	Monoclinic
Space group	*C*2/*c*	*P*2/*c*	*P*2/*c*	$P2_1/c$	$P2_1/n$
a (Å)	17.4708(16)	13.1785(4)	13.592(3)	9.7019(12)	10.0908(6)
b (Å)	7.9414(7)	9.3729(3)	9.3991(19)	19.475(2)	36.845(2)
c (Å)	9.9424(9)	16.2115(5)	16.089(3)	35.316(5)	18.3609(10)
β (°)	121.725(4)	98.098(2)	97.02(3)	90.429(6)	96.755(3)
Volume ($Å^3$)	1173.32(19)	1982.49(11)	2040.0(7)	6672.6(14)	6779.1(7)
Z	4	4	4	2	2
Density (mg m^{-3})	1.676	1.549	1.795	1.490	1.487
Abs. coeff. (mm^{-1})	1.890	1.155	4.778	2.949	2.901
F(000)	604	964	1108	3072	3096
Crystal size (mm^3)	0.349 × 0.318 × 0.224	0.06 × 0.04 × 0.04	0.666 × 0.646 × 0.578	0.687 × 0.284 × 0.250	0.8 × 0.4 × 0.4
N_{ref}	19 163	7648	4831	151 106	78 576
GOF on F^2	1.135	1.062	1.127	1.114	1.017
Completeness	99.8%	100.00%	100%	100%	99.9%
R [$I > 2\sigma(I)$]: R_1 [a] (wR_2 [b])	0.0251 (0.0718)	0.0229 (0.0564)	0.0915 (0.2291)	0.0676 (0.1622)	0.0577 (0.1208)
R indices (all data) R_1 [a] (wR_2 [b])	0.0256 (0.0721)	0.0265 (0.0580)	0.0935 (0.2309)	0.0763 (0.1667)	0.1133 (0.1404)

[a] $R_1 = \sum||F_o| - |F_c||/\sum|F_o|$. [b] $wR_2 = [\sum[w(F_o^2 - F_c^2)^2]/\sum[w(F_o^2)^2]]^{\frac{1}{2}}$, $w = 1/[\sigma^2(F_o^2) + (aP)^2 + bP]$, where $P = [\max(F_o^2 \text{ or } 0) + 2(F_c^2)]/3$.

Special refinement details are summarized herein. In the structure of **1**, the data were refined as a two-component pseudo-merohedral twin; the refined fractional contribution of the minor component is 22.51%. Two reflections were omitted due to interference from the beam stop (0 0 2 and 1 0 0). In the structure of **2**, the data were refined as a two-component pseudo-merohedral twin; the refined fractional contribution of the minor component is 44.21%. In the structure of **3**, several of the α-, β-, and γ-carbon atoms, as well as several nitrogen atoms of the of H_2bip ligands are disordered across two positions (labelled A and B) for N7/C9/C10/C11, N11/C17/C18/C19, N23/C41/C42/C43, and N24/C46/C47/C48; these refined to 56.25% and 43.75%, respectively. In the structure of **4**, severely disordered acetonitrile co-solvent was present in the interstitial lattice voids. PLATON SQUEEZE was implemented to remove the disordered 93 electrons from the solvent accessible void of 392 Å^3.[57] This is assumed to be four equivalents of acetonitrile molecules (22 electron count); we find $\frac{1}{4}$ of water per Co in the structure; the solvent mass was used in the calculation of the formula weight of **4**.

Magnetic measurements

Solid-state magnetic susceptibility measurements were performed using a Quantum Design model MPMS-XL SQUID magnetometer on crystalline samples, prepared under a dinitrogen atmosphere. Microcrystalline samples were loaded in polyethene bags and sealed in the glovebox, inserted into a straw and transported to the SQUID magnetometer under dinitrogen. Ferromagnetic impurities were checked through a variable field analysis at 100 K: no significant impurities were detected (Fig. S7 and S8†). Data were corrected for the magnetization of the sample holder; diamagnetic corrections of the sample were applied using Pascal's constants.[58] The temperature dependencies of magnetic susceptibilities of the compounds were recorded between 1.8 and 300 K under 1000 Oe dc applied field. Magnetization measurements were collected in the temperature range 1.8 K to 12 K at applied dc fields of 10, 20, 30, 40, and 50 kOe (Fig. S9†). Molar susceptibility values take into account all solvate molecules as determined by X-ray diffraction studies. Temperature-dependent magnetic susceptibility data were fit with the program PHI[23] (eqn (1)) and the reduced field magnetization data were fit with ANISOFIT 2.0[21] (eqn (2)) to quantify the magnetic g and anisotropy parameters with the help of the following spin Hamiltonians.

$$\hat{H} = \mu_B g\hat{S}\cdot\bar{B} + D(\hat{S}_z{}^2 - 1/3\hat{S}(\hat{S}+1)) + E(\hat{S}_x{}^2 - \hat{S}_y{}^2) \quad (1)$$

$$\hat{H} = \mu_B g\hat{S}\cdot\bar{B} + D\hat{S}_z{}^2 + E(\hat{S}_x{}^2 - \hat{S}_y{}^2) \quad (2)$$

The initial values obtained for axial (D) and rhombic (E) anisotropy parameters gave $|E/D| > 1/3$ for compounds **1** and **2** (Table S1†); thus the D and E parameters were re-determined by the customary assignment of the principal values of D-tensor.[24,25] Alternating current (AC) magnetic susceptibility measurements were performed on samples of all four compounds at temperatures between 1.8 K and 12 K, with an oscillating field of 4 Oe.

Other physical methods

Infrared spectra were measured with a Nicolet 380 FT–IR under a dinitrogen flow using an ATR attachment with a ZnSe crystal in the range 400 cm^{-1}–4000 cm^{-1}. Solution electronic absorption spectra were obtained with a Hewlett-Packard 8453 spectrophotometer in quartz cuvettes with 1 cm path lengths; all experiments were performed at room temperature. Elemental analyses were performed by Robertson Microlit Laboratories, Inc. in Madison, NJ.

Conflicts of interest

The authors have no conflicts to declare.

Acknowledgements

We thank Colorado State University and the National Science Foundation (CHE-1363274, CHE-1800554, and CHE-1956399) for financial support. We acknowledge Prof. C. M. Elliott (deceased) for providing 4,4′-methyl-2,2′-dipyridyl (Me_2bpy) ligand,[42] and Prof. K. Kittilstved for insightful discussions.

Notes and references

1 J. M. Frost, K. L. M. Harriman and M. Murugesu, *Chem. Sci.*, 2016, **7**, 2470–2491.
2 S. Tripathi, A. Dey, M. Shanmugam, R. S. Narayanan and V. Chandrasekhar, *Cobalt(II) Complexes as Single-Ion Magnets, Organometallic Magnets*, Springer, 2019, vol. 64, pp. 35–75.
3 G. A. Craig and M. Murrie, *Chem. Soc. Rev.*, 2015, **44**, 2135.
4 A. K. Bar, C. Pichon and J.-P. Sutter, *Coord. Chem. Rev.*, 2016, **308**, 346–380.
5 (*a*) Y.-Z. Zhang, S. Gómez-Coca, A. J. Brown, M. R. Saber, X. Zhang and K. R. Dunbar, *Chem. Sci.*, 2016, **7**, 6519–6527; (*b*) M. Feng and M.-L. Tong, *Chem. – Eur. J.*, 2018, **24**, 7574–7594; (*c*) Y. P. Tupolova, I. N. Shcherbakov, D. V. Korchagin, V. V. Tkachev, V. E. Lebedev, L. D. Popov, K. V. Zakharov, A. N. Vasiliev, A. V. Palii and S. M. Aldoshin, *J. Phys. Chem. C*, 2020, **124**, 25957–25966; (*d*) A. Świtlicka, B. Machura, M. Penkala, A. Bieńko, D. C. Bieńko, J. Titiš, C. Rajnák, R. Boča and A. Ozarowski, *Inorg. Chem. Front.*, 2020, **7**, 2637–2650; (*e*) Y.-F. Deng, M. K. Singh, D. Gan, T. Xiao, Y. Wang, S. Liu, Z. Wang, Z. Ouyang, Y.-Z. Zhang and K. R. Dunbar, *Inorg. Chem.*, 2020, **59**, 7622–7630.
6 H.-H. Cui, Y.-Q. Zhang, X.-T. Chen, Z. Wang and Z.-L. Xue, *Dalton Trans.*, 2019, **48**, 10743–10752.
7 D. Sertphon, K. S. Murray, W. Phonsri, J. Jover, E. Ruiz, S. G. Telfer, A. Alkaş, P. Harding and D. J. Harding, *Dalton Trans.*, 2018, **47**, 859–867.
8 E. Ferentinos, M. Xu, A. Grigoropoulos, I. Bratsos, C. P. Raptopoulou, V. Psycharis, S.-D. Jiang and P. Kyritsis, *Inorg. Chem. Front.*, 2019, **6**, 1405–1414.
9 S. Gómez-Coca, A. Urtizberea, E. Cremades, P. J. Alonso, A. Camón, E. Ruiz and E. Luis, *Nat. Commun.*, 2014, **5**, 4300.

10 J. Vallejo, I. Castro, R. Ruiz-García, J. Cano, M. Julve, F. Lloret, G. De Munno, W. Wernsdorfer and E. Pardo, *J. Am. Chem. Soc.*, 2012, **134**, 15704–15707.
11 Z. Ni and M. P. Shores, *J. Am. Chem. Soc.*, 2009, **131**, 32–33.
12 Z. Ni, A. M. McDaniel and M. P. Shores, *Chem. Sci.*, 2010, **1**, 615–621.
13 Z. Ni and M. P. Shores, *Inorg. Chem.*, 2010, **49**, 10727–10735.
14 Z. Ni, S. R. Fiedler and M. P. Shores, *Dalton Trans.*, 2011, **40**, 944–950.
15 A. J. Downs and C. J. Adams, Pergamon text for Inorganic Chemistry, in *The Chemistry of Chlorine, Bromine, Iodine and Astatine*, Pergamon Press, 1973, vol. 7, pp. 1277–1278.
16 (*a*) P. J. Desrochers, J. Telser, S. A. Zvyagin, A. Ozarowski, J. Krzystek and D. A. Vicic, *Inorg. Chem.*, 2006, **45**, 8930–8941; (*b*) C. Duboc, T. Phoeung, S. Zein, J. Pécaut, M.-N. Collomb and F. Neese, *Inorg. Chem.*, 2007, **46**, 4905–4916.
17 H. L. Karunadasa, K. D. Arquero, L. A. Berben and J. R. Long, *Inorg. Chem.*, 2010, **49**, 4738–4740.
18 W. Huang, T. Liu, D. Wu, J. Cheng, Z. W. Ouyangc and C. Duan, *Dalton Trans.*, 2013, **42**, 15326–15331.
19 M. Idešicová, J. Titiš, J. Krzystek and R. Boča, *Inorg. Chem.*, 2013, **52**, 9409–9417.
20 R.-C. Yang, D.-R. Wang, J.-L. Liu, Y.-F. Wang, W.-Q. Lin, J.-D. Leng and A.-J. Zhou, *Chem. – Asian J.*, 2019, **14**, 1467–1471.
21 J. M. Zadrozny, J. Telser and J. R. Long, *Polyhedron*, 2013, **64**, 209–217.
22 S. Ziegenbalg, D. Hornig, H. Görls and W. Plass, *Inorg. Chem.*, 2016, **55**, 4047–4058.
23 N. F. Chilton, R. P. Anderson, L. D. Turner, A. Soncini and K. S. Murray, *J. Comput. Chem.*, 2013, **34**, 1164–1175.
24 M. P. Shores, J. J. Sokol and J. R. Long, *J. Am. Chem. Soc.*, 2002, **124**, 2279.
25 R. Boča, *Theoretical Foundations of Molecular magnetism*, Elsevier, 1999, pp. 424–425.
26 R. Boča, in *Magnetic Functions Beyond the Spin-Hamiltonian*, ed. D. M. P. Mingos, Springer Berlin Heidelberg, Berlin, Heidelberg, 2006, pp. 1–264.
27 R. Boča, C. Rajnák, J. Moncol, J. Titiš and D. Valigura, *Inorg. Chem.*, 2018, **57**, 14314–14321.
28 I. Nemec, R. Herchel and Z. Trávníček, *Dalton Trans.*, 2018, **47**, 1614–1623.
29 J. Titiš and R. Boča, *Inorg. Chem.*, 2011, **50**, 11838–11845.
30 L. Tesi, E. Lucaccini, I. Cimatti, M. Perfetti, M. Mannini, M. Atzori, E. Morra, M. Chiesa, A. Caneschi, L. Sorace and R. Sessoli, *Chem. Sci.*, 2016, **7**, 2074–2083.
31 M. Atzori, L. Tesi, S. Benci, A. Lunghi, R. Righini, A. Taschin, R. Torre, L. Sorace and R. Sessoli, *J. Am. Chem. Soc.*, 2017, **139**, 4338–4341.
32 R. Boča, C. Rajnák, J. Moncol, J. Titiš and D. Valigura, *Inorg. Chem.*, 2018, **57**, 14314–14321.
33 A. Świtlicka, J. Palion-Gazda, B. Machura, J. Cano, F. Lloret and M. Julve, *Dalton Trans.*, 2019, **48**, 1404–1417.
34 L. Tesi, E. Lucaccini, I. Cimatti, M. Perfetti, M. Mannini, M. Atzori, E. Morra, M. Chiesa, A. Caneschi, L. Sorace and R. Sessoli, *Chem. Sci.*, 2016, **7**, 2074–2083.
35 M. Atzori, E. Morra, L. Tesi, A. Albino, M. Chiesa, L. Sorace and R. Sessoli, *J. Am. Chem. Soc.*, 2016, **138**, 11234–11244.
36 M. Ding, G. E. Cutsail, D. Aravena, M. Amoza, M. Rouzières, P. Dechambenoit, Y. Losovyj, M. Pink, E. Ruiz, R. Clérac and J. M. Smith, *Chem. Sci.*, 2016, **7**, 6132–6140.
37 I. Bhowmick, A. J. Roehl, J. R. Neilson, A. K. Rappé and M. P. Shores, *Chem. Sci.*, 2018, **9**, 6564–6571.
38 Y. Terasakia and S. Kaizaki, *J. Chem. Soc., Dalton Trans.*, 1995, 2837–2831.
39 K. Kurzak, B. Kurzak, A. Kamecka and A. Woźna, *J. Solution Chem.*, 2001, **30**, 1051–1064.
40 H. Souissi and S. Kammoun, *Mater. Sci. Appl.*, 2011, **2**, 1121–1126.
41 B. N. Figgis and M. A. Hitchman, *Ligand Field theory and its application*, 2000, p. 71.
42 M. Gerloch, *Magnetism and Ligand-field Analysis*, 1983, pp. 525, 545 and 556.
43 P. D. Day, *Electronic Structure and Magnetism of Inorganic Compounds*, 1982, p. 152.
44 G. L. Miessler, *Inorganic Chemistry*, 4th edn, 2010, p. 399.
45 C. E. Schaffer, The Angular Overlap Model of the Ligand Field Theory and Applications, *Pure Appl. Chem.*, 1970, **24**, 361–392.
46 A. K. Mondal, M. Sundararajan and S. Konar, *Dalton Trans.*, 2019, **47**, 3745–3754.
47 I. Krivokapic, M. Zerara, M. L. Daku, A. Vargas, C. Enachescu, C. Ambrus, P. Tregenna-Piggott, N. Amstutz, E. Krausz and A. Hauser, *Coord. Chem. Rev.*, 2007, **251**(3–4), 364–378.
48 S. Gomez-Coca, E. Cremades, N. Aliaga-Alcalde and E. Ruiz, *J. Am. Chem. Soc.*, 2013, **135**, 7010–7018.
49 H. Oshio and M. Nakano, *Chem. – Eur. J.*, 2005, **11**, 5178–5185.
50 M. G. Burnett, V. McKee and S. M. Nelson, *J. Chem. Soc., Dalton Trans.*, 1981, 1492.
51 C. M. Elliott, R. A. Freitag and D. D. Blaney, *J. Am. Chem. Soc.*, 1985, **107**, 4655–4662.
52 J. Cosier and A. M. Glazer, A nitrogen-gas-stream cryostat for general X-ray diffraction studies, *J. Appl. Crystallogr.*, 1986, **19**, 105–107.
53 Bruker, *SAINT, v.8.38A*, Bruker AXS Inc., Madison, WI, USA, 2016.
54 G. M. Sheldrick, *SADABS Version 2.03*, Bruker Analytical X-Ray Systems, Madison, WI, 2000.
55 L. Krause, R. Herbst-Irmer, G. M. Sheldrick and D. Stalke, Beyond the international year of crystallography, *J. Appl. Crystallogr.*, 2015, **48**, 3–10.
56 G. M. Sheldrick, Crystal structure refinement with SHELXL, *Acta Crystallogr., Sect. C: Struct. Chem.*, 2015, **71**, 3–8.
57 A. L. Spek, PLATON SQUEEZE: a tool for the calculation of the disordered solvent contribution to the calculated structure factors, *Acta Crystallogr., Sect. C: Struct. Chem.*, 2015, **71**, 9–18.
58 G. A. Bain and J. F. Berry, *J. Chem. Educ.*, 2008, **85**, 532–536.

